

Experimental and simulation study of a capacitively coupled oxygen discharge driven by tailored voltage waveforms

Aranka Derzsi¹, Trevor Lafleur², Jean-Paul Booth², Ihor Korolov¹ and Zoltán Donkó¹

¹ Institute for Solid State Physics and Optics, Wigner Research Centre for Physics, Hungarian Academy of Sciences, 1121 Budapest, Konkoly Thege Miklós str. 29-33, Hungary

² Laboratoire de Physique des Plasmas, Ecole Polytechnique-CNRS-Univ Paris-Sud-UPMC, 91128 Palaiseau, France

E-mail: derzsi.aranka@wigner.mta.hu

Received 30 July 2015, revised 4 October 2015

Accepted for publication 26 October 2015

Published 1 December 2015



CrossMark

Abstract

We report experimental and particle-based kinetic simulation studies of low-pressure capacitively coupled oxygen plasmas driven by tailored voltage waveforms that consist of up to four harmonics of base frequency 13.56 MHz. Experimentally determined values of DC self-bias and electrical power deposition, as well as flux density and flux-energy distribution of the positive ions at the grounded electrode are compared with simulation data for a wide range of operating conditions. Very good agreement is found for self-bias and flux-energy distribution of the positive ions at the electrodes, while a fair agreement is reached for discharge power and ion flux data. The simulated spatial and temporal behaviour of the electric field, electron density, electron power absorption, ionization rate and mean electron energy shows a transition between sheath expansion heating and drift-ambipolar discharge modes, induced by changing either the number of harmonics comprising the excitation waveform or the gas pressure. The simulations indicate that under our experimental conditions the plasma operates at high electronegativity, and also reveal the crucial role of $O_2(a^1\Delta_g)$ singlet metastable molecules in establishing discharge behavior via the fast destruction of negative ions within the bulk plasma.

Keywords: capacitive plasma, oxygen discharge, tailored voltage waveform

(Some figures may appear in colour only in the online journal)

1. Introduction

Capacitively coupled plasmas (CCPs) operating in various gases are important in many high-tech applications, including etching and deposition of thin films and modification of surface properties (see for example [1, 2]). Oxygen and oxygen-containing plasmas, in particular, have been applied for stripping of polymer photoresist films, functionalization of fibre surfaces [3], improvement of properties of biocompatible surfaces [4] and of resistive switching memory circuits [5], and fabrication of nanofluidic devices [6] and gas sensors based on carbon nanotube network films [7], as well

as transparent and conductive thin layers [8]. The physics and chemistry of capacitively coupled radio frequency (RF) plasmas in oxygen have been the subject of many studies, both experimental and via modelling, during recent decades. The particle-in-cell method combined with Monte Carlo treatment of collision processes (known as PIC/MCC [9]) has played an important role in modelling studies where a kinetic description of particle transport is necessary [10–12]. Previous modelling studies have revealed details of the plasma dynamics [13], and explained the pressure dependence of electron energy distributions in both capacitively and inductively coupled oxygen plasmas [14]. A sequence of three papers [15–17] discussed

the modelling issues, analyzed the spatiotemporally resolved optical emission patterns of the plasma and gave a comparison between experimental and modelling results in low-pressure oxygen CCPs, respectively. The effect of magnetic fields on the generation and confinement of low-pressure capacitive oxygen plasmas, motivated by the optimization of ion-etching applications, was investigated in [18], while the role of atomic oxygen was studied in [19]. The influence of external control parameters on the electron density in low-pressure capacitively coupled oxygen discharges was investigated in [20, 21]. The appearance of an instability (characteristic for electro-negative plasmas [22]) was studied in an oxygen CCP in [23], where periodic oscillations in the sub-kHz frequency range were found to be excited. Observation of the optical emission patterns revealed that the plasma oscillates between high- and low-electronegativity modes within the fluctuation cycles. Electron attachment/detachment processes were shown to play a central role in generating this instability [23]. Negative ions in O₂ plasmas have been studied experimentally using laser photodetachment combined with microwave interferometry, accompanied by particle simulations [24, 25].

In most plasma processing applications the flux and energy of ions reaching the electrode (target) surfaces are of primary importance. In recent years a number of schemes have been proposed for the separate control of these properties. The first scheme that was proposed uses excitation of the plasma by two, or more, significantly different radio frequencies (e.g. 2 + 27 MHz, 1 + 100 MHz) [26–30]. Under such conditions the plasma density and (strongly linked) ion flux are controlled by the amplitude of the high-frequency component of the driving waveform, while the ion energy is primarily set by the amplitude of the low-frequency component. The degree of control separation is limited by coupling effects and can be achieved only within narrow windows of the discharge operating parameters [31]. In another scheme, which has become known as the ‘electrical asymmetry effect’ (EAE), dual-frequency excitation is performed using two consecutive harmonics (e.g. 13.56 + 27.12 MHz) [32–37]. This type of excitation allows the ion energy to be tuned by the phase angle between the driving harmonics, due to the varying DC self-bias that is caused by the electrically asymmetric excitation waveform, while the ion flux remains nearly constant (and is defined by the amplitudes of the driving harmonics). The EAE has been thoroughly studied in recent years, and in particular the number of consecutive harmonics has been increased above two, both in experiments [38] and in simulations [39].

It has been realized that, when using such multi-harmonic waveforms, further degrees of freedom can be obtained by changing both the amplitudes and the phases, giving control of the discharge characteristics over a wide domain. Such waveforms (which include pulse-like [40] and sawtooth-like [41] shapes, among others) have become known as ‘customized’ or ‘tailored’ voltage waveforms; for a summary of progress see the review of Lafleur [42] and references therein.

While plasma sources employing tailored voltage waveform excitation are now being developed for laboratory-scale and industrial surface processing, further investigation is necessary to uncover the details of discharge operation at the level

of elementary processes, particularly in molecular gases. The aim of the present paper is to contribute to this understanding by reporting a combined experimental and simulation study of a low-pressure oxygen CCP, excited by tailored voltage waveforms consisting of a base harmonic and a number of additional higher harmonics. Our methods (the experimental setup, discharge model and simulation method) are described in section 2. The experimental and simulation results are presented and compared to each other in section 3, and a short summary of the work is given in section 4.

2. Methods

The experimental setup is described in section 2.1, while the details of the discharge model and simulation method are presented in section 2.2. The general form of the multifrequency tailored voltage waveforms (as also used here) is

$$\phi(t) = \sum_{k=1}^N \phi_k \cos(2\pi k f_1 t + \Theta_k), \quad (1)$$

where N is the number of harmonics that have amplitudes and phase angles, ϕ_k and Θ_k ($k = 1 \dots N$), respectively, and f_1 is the fundamental RF frequency.

Here we apply two classes of waveforms:

- (i) ‘Peaks’ and ‘valleys’ waveforms: In the above form of the driving voltage waveform the amplitudes of the individual harmonics are set according to the equations

$$\phi_k = \phi_0 \frac{N - k + 1}{N}, \quad \phi_0 = \frac{2N}{(N + 1)^2} \phi_{PP}, \quad (2)$$

where ϕ_{PP} is the peak-to-peak voltage. The ‘peaks’ voltage waveforms are generated by setting all phase angles to zero, while ‘valleys’-type waveforms are obtained by changing the phase angles of all the even harmonics to $\Theta_k = \pi$. Figure 1(a) illustrates ‘peaks’-type voltage waveforms given by (1) for different numbers of harmonics, for $\phi_{PP} = 150$ V.

- (ii) EAE waveforms: To study the effect of phase variation we adopt the dual-frequency driving voltage waveform

$$\phi(t) = \phi_{12} [\cos(2\pi f_1 t + \Theta_1) + \cos(4\pi f_1 t)]. \quad (3)$$

Examples of waveforms generated in this way are displayed in figure 1(b) for different phase angles and $\phi_{12} = \phi_1 = \phi_2 = 50$ V.

2.1. Experiment

Experiments were performed in the DRACULA CCP plasma reactor previously described in [43] and shown schematically in figure 2. The cylindrically symmetric reactor consists of two aluminium electrodes each 50 cm in diameter, separated by a distance of $L = 2.5$ cm. The bottom electrode is powered, while the top electrode is grounded. The plasma between the electrodes is radially bounded by a large Pyrex cylinder and a thick Teflon dielectric, thus ensuring that the plasma ‘sees’

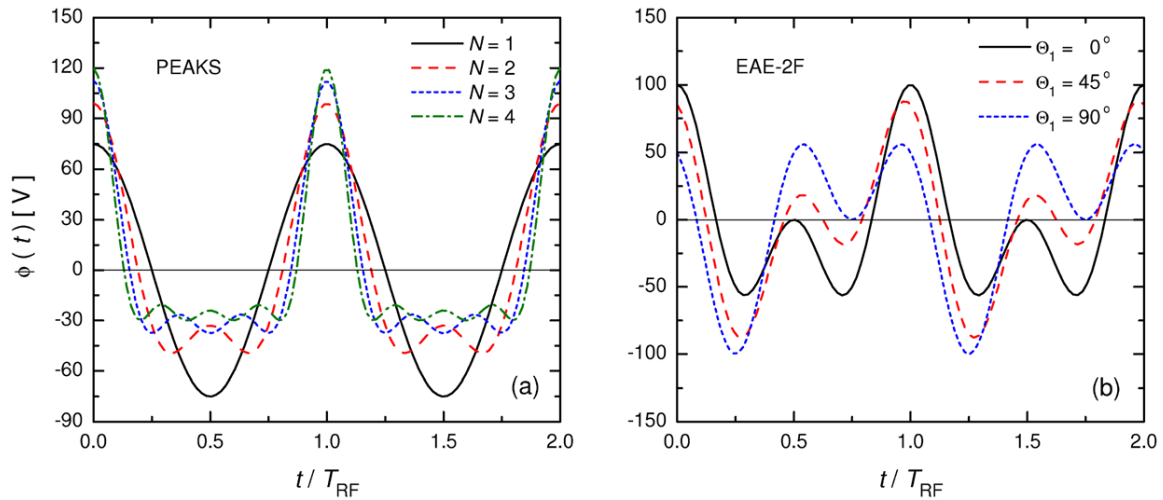


Figure 1. Generator waveforms for (a) ‘peaks’-type excitation, for $\phi_{pp} = 150$ V. (‘valleys’-type voltage waveforms are mirror images of the displayed waveforms with respect to $\phi = 0$.) (b) Generator waveforms for dual-frequency excitation used for studies of the EAE, with $\phi_{12} = \phi_1 = \phi_2 = 50$ V. The time axis covers two periods (T_{RF}) of the fundamental RF frequency. Note that, generally, the discharge voltage waveforms include an additional DC self-bias for $N > 1$, which is not shown here.

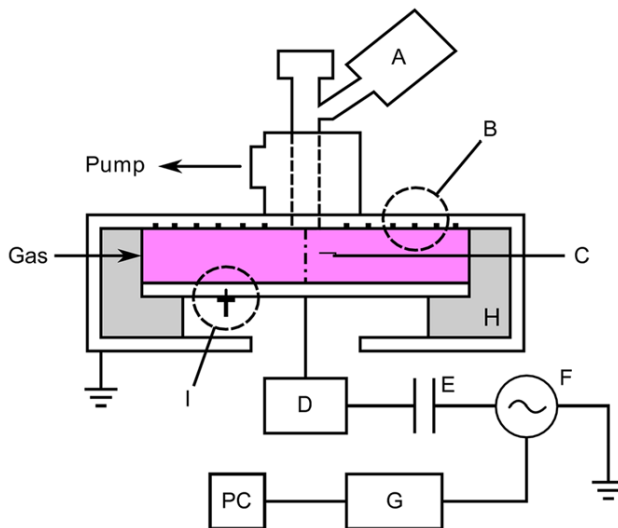


Figure 2. Schematic of the DRACULA plasma reactor, showing the Hidden mass spectrometer (A), ion flux probe array (B), hairpin resonator probe (C), SOLAYL VI probe (D), blocking capacitor (4.5 nF; E), RF power amplifier (F), arbitrary function generator (G), dielectric spacers between the powered and grounded electrodes (H), and high-voltage probe (I).

almost equal electrode areas. The chamber is pumped with a rotary/turbomolecular pump system, and pressure is measured using both ion and Baratron gauges. Oxygen is injected into the reactor via a side port of the chamber and the flow rate is set using a mass flow controller. The powered electrode is connected to a class A broadband RF power amplifier via a 4.5 nF bias capacitor. The amplifier is controlled by an arbitrary function generator and a PC using a LABVIEW program that creates and sends the desired voltage waveforms. The frequency response of the reactor and the plasma impedance in general distorts this waveform, and so a Fourier transform feedback technique [43, 44] is used to ensure that the desired

waveforms can be reproduced on the powered electrode. A SOLAYL voltage-current probe (described in detail in [45]) is placed between the powered electrode and the bias capacitor to monitor the discharge current and power. The discharge voltage and the DC self-bias are measured with a 100 : 1 high-voltage probe connected directly to the powered electrode.

The ion flux energy distribution function (IFEDF) is measured with a HIDDEN EQP mass/energy spectrometer. The spectrometer entrance orifice is embedded in the grounded electrode and aligned with the axis of the reactor. In order to avoid the convolution of the unknown ion distribution with the energy-dependent acceptance angle of the spectrometer (which requires trajectory simulations) [46, 47], the focusing electrodes are turned off and only ions in a narrow acceptance angle of about 2° are measured.

The experimental system also allows the determination of the flux of the ions to the grounded electrode with 16 planar probes embedded in the electrode along a common diametric line. In this paper we present particle simulation results and compare them to experimentally measured self-bias voltage, power absorbed by the discharge, ion flux and flux energy distribution of ions. This comparison of multiple characteristics provides a rigorous check of the collisional model underlying the simulations.

2.2. Modelling of the oxygen radio frequency plasma

The modelling of oxygen plasmas is challenging due to their complicated chemistry which involves a number of different species and reaction channels (see for example [48–51]). Selecting relevant reactions, as well as analyzing their importance and the sensitivity of the results to the reaction data used is a laborious task [52].

There are several sets of processes and related cross sections/rate coefficients available in the literature for O_2 plasmas [10–12, 15, 53]. These sets differ in many respects: in the number of species and reaction processes considered, in the values of the

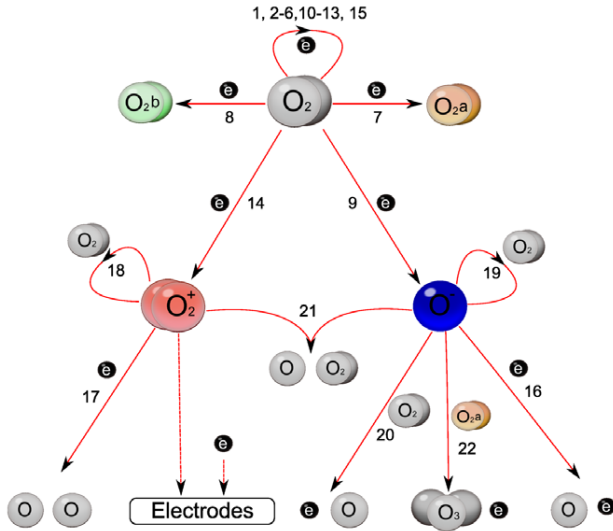


Figure 3. Scheme of elementary processes considered in our model of the oxygen plasma. Arrows indicate reaction channels, the numbers beside the arrows refer to entries in table 1.

cross sections, and in the handling of certain processes. Most models consider electrons, O_2^+ ions and O^- ions as the principal charged species. In a recent study [12] a critical comparison between computational results obtained using different reaction data and different simulation codes was presented. This work also considered O^+ ions, claiming that they are increasingly important at higher pressures. Although the process and cross section set given in [12] is probably the most comprehensive to date, the results were not compared to experimental data. Notably, the detachment reaction of O^- ions by collision with $O_2(a^1\Delta_g)$ molecules [54, 55] was ignored. However, $O_2(a^1\Delta_g)$ can be present with appreciable concentration, and consequently the charged particle densities are likely overestimated. Nevertheless, the authors acknowledged that this associative detachment reaction is an important subject for future work. As we will see later, this process plays a vital role (as recognized by [15, 56, 57]) in the charged particle balance of the plasma.

The set of elementary processes considered in this work is illustrated in figure 3, with details given in table 1.

The process list and cross sections adopted are largely based on the well-established ‘xpdp1’ set [10]. Only a few changes have been introduced to refine some of the processes and corresponding data (see below). The collision processes between electrons and O_2 molecules (see table 1) include elastic scattering, excitation to rotational, vibrational and electronic levels, ionization, dissociative excitation, and dissociative attachment (processes 1–15). Electron impact detachment (process 16) and dissociative recombination (process 17) are also accounted for. For O_2^+ ions, elastic collisions with O_2 (including charge exchange, see the footnote of table 1) are included (process 18). For O^- ions we consider elastic scattering with O_2 , detachment by collisions with electrons and O_2 molecules, and mutual neutralization with O_2^+ ions (processes 19–21, respectively), as well as the detachment reaction with singlet delta oxygen molecules, $O_2(a^1\Delta_g)$, of which the density may be significant in CCPs (process 22).

Compared to the original ‘xpdp1’ cross section set we: replace the elastic collision cross section with the elastic momentum transfer cross section of Biagi [58] and use, accordingly, isotropic electron scattering; replace the original xpdp1 ionization cross section with that recommended by Gudmundsson [12]; and adopt all the cross sections for heavy particle processes (ion–molecule and ion–ion collisions) from Gudmundsson’s work [12], except for process 22, for which we use the cross section given in [15].

We note that metastable $O_2(a^1\Delta_g)$ molecules, having a long lifetime, play an important role in the plasma chemistry, and without process 22 the calculations may overestimate the positive and negative ion densities significantly [56, 57]. Unfortunately, it is difficult to calculate the $O_2(a^1\Delta_g)$ density self-consistently. Therefore we follow a procedure that assumes a homogeneous spatial density of these molecules and estimate their density from a simple balance equation. The source of $O_2(a^1\Delta_g)$ molecules is electron impact excitation of O_2 (process 7), and the rate of this process is readily available from the simulations. We assume that the molecules are predominantly lost by quenching at the electrodes, with a loss rate k that, according to [59], is given as

$$\frac{1}{k} = \frac{\Lambda_0^2}{D} + \frac{V}{A} \frac{2(2-\alpha)}{\bar{v}\alpha}, \quad (4)$$

where α is the surface quenching probability, D is the diffusion coefficient of $O_2(a^1\Delta_g)$ in O_2 (which we take to be equal to the self-diffusion coefficient of O_2 , given in [60]), V/A is the volume to surface area of the reactor, \bar{v} is the mean thermal velocity (which we calculate from the gas temperature), and

$$\frac{1}{\Lambda_0^2} = \left(\frac{\pi}{L}\right)^2 + \left(\frac{2.4}{R}\right)^2, \quad (5)$$

where $R = 25$ cm is the electrode radius. At equilibrium, the balance equation for the density, n_a , of $O_2(a^1\Delta_g)$ is

$$0 = \left(\frac{\partial n_a}{\partial t}\right) = \left(\frac{\partial n_a}{\partial t}\right)^+ - \left(\frac{\partial n_a}{\partial t}\right)^-, \quad (6)$$

where the first (creation) term on the right-hand side is the rate of process 7, while the loss term is

$$\left(\frac{\partial n_a}{\partial t}\right)^- = kn_a, \quad (7)$$

which allows the calculation of n_a from k .

The computational description of the oxygen CPP, driven by tailored RF waveforms is based on PIC/MCC [9]. Our code is one-dimensional (1D) in space and 3D in velocity space. The electrodes are assumed to be plane and parallel. We use a fixed gas temperature of $T_g = 300$ K, justified by the low power levels. Both the electron reflection coefficient at the electrodes and the secondary electron yield are set to zero. We note that in CCPs secondary electrons, emitted from the electrodes, may play an important role at higher pressures. However, under the conditions covered in this study, their role was found to be less important, since the discharge voltage did not exceed the relatively low value of 250V peak-to-peak. Under such conditions

Table 1. List of collisions considered in the simulation.

#	Reaction	Process	References
1	$e^- + O_2 \longrightarrow O_2 + e^-$	Elastic scattering	[58]
2	$e^- + O_2(r = 0) \longrightarrow e^- + O_2(r > 0)$	Rotational excitation	xpdp1 ^a
3	$e^- + O_2(v = 0) \longrightarrow e^- + O_2(v = 1)$	Vibrational excitation	xpdp1
4	$e^- + O_2(v = 0) \longrightarrow e^- + O_2(v = 2)$	Vibrational excitation	xpdp1
5	$e^- + O_2(v = 0) \longrightarrow e^- + O_2(v = 3)$	Vibrational excitation	xpdp1
6	$e^- + O_2(v = 0) \longrightarrow e^- + O_2(v = 4)$	Vibrational excitation	xpdp1
7	$e^- + O_2 \longrightarrow e^- + O_2(a^1\Delta_g)$	Metastable excitation (0.98 eV)	xpdp1
8	$e^- + O_2 \longrightarrow e^- + O_2(b^1\Sigma_g)$	Metastable excitation (1.63 eV)	xpdp1
9	$e^- + O_2 \longrightarrow O + O^-$	Dissociative attachment	xpdp1
10	$e^- + O_2 \longrightarrow e^- + O_2$	Excitation (4.5 eV)	xpdp1
11	$e^- + O_2 \longrightarrow O(^3P) + O(^3P) + e^-$	Dissociation (6.0 eV)	xpdp1
12	$e^- + O_2 \longrightarrow O(^3P) + O(^1D) + e^-$	Dissociation (8.4 eV)	xpdp1
13	$e^- + O_2 \longrightarrow O(^1D) + O(^1D) + e^-$	Dissociation (9.97 eV)	xpdp1
14	$e^- + O_2 \longrightarrow O_2^+ + e^- + e^-$	Ionization	[12]
15	$e^- + O_2 \longrightarrow e^- + O + O(3p^3P)$	Dissociative excitation (14.7 eV)	xpdp1
16	$e^- + O^- \longrightarrow e^- + e^- + O$	Electron impact detachment	xpdp1
17	$e^- + O_2^+ \longrightarrow O(^3P) + O(^1D)$	Dissociative recombination	xpdp1
18	$O_2^+ + O_2 \longrightarrow O_2 + O_2^+$	Elastic scattering ^b	[12]
19	$O^- + O_2 \longrightarrow O^- + O_2$	Elastic scattering	[12]
20	$O^- + O_2 \longrightarrow O + O_2 + e^-$	Detachment	[12]
21	$O^- + O_2^+ \longrightarrow O + O_2$	Mutual neutralization	[12]
22	$O^- + O_2(a^1\Delta_g) \longrightarrow O_3 + e^-$	Associative detachment	[15]

^a More detailed information about the ‘xpdp1’ set, including references to cross section data, can be found in [10, 12].

^b In [12] this process is referred to as charge exchange and an additional process of isotropic elastic scattering with a cross section that has 50% magnitude of the charge exchange cross section is additionally included. Here, we use the same values for the cross sections, but follow the recommendation of Phelps [61] for the terminology and call this process elastic scattering, since charge exchange is also an elastic process.

electron multiplication within the electrode sheaths is small, as confirmed in our simulations. The computational grid has $N_g = 200$ points between the electrodes and the simulation time step is set to $\Delta t = T_{RF}/N_t$, where T_{RF} is the period of the fundamental RF frequency (13.56 MHz), and typically $N_t = 4000$.

These parameter values fulfil the convergence criteria (the time step is small enough to resolve electron plasma oscillations, the computational mesh is dense enough to resolve the Debye length) of the PIC scheme. The relatively small number of mesh points aids the fulfilment of the Courant condition and does not limit the resolution of the characteristic structure of the discharge. The number of superparticles was around 10^5 for each species (using different superparticle weights for the different species), which resulted in a convergence time of about 100h on a single CPU.

When two or more RF harmonics are applied for the excitation of the plasma, the self-bias η is determined in an iterative way, by adjusting its value to achieve equality of electron and ion fluxes to each of the electrodes over one period of the fundamental driving frequency [62].

We note that by ‘reversing’ the waveform shape (peaks ↔ valleys): the bias changes sign, but has the same magnitude, and the plasma changes to its mirror image with respect to the midplane. This expected behaviour was confirmed for a few selected cases in the simulations. As a single simulation gives access to the ion fluxes and energy distributions at both electrodes (while in the experiment these characteristics can only

be obtained at the grounded side), it is sufficient to simulate discharges excited by only one, e.g. the ‘peaks’-type waveforms.

3. Results

In the following we present a detailed characterization of the oxygen CCP driven by ‘peaks’ and ‘valleys’ RF waveforms according to equation (1), operating in the pressure range $50 \text{ mTorr} < p < 380 \text{ mTorr}$. Subsequently, we illustrate the effect of varying the phase angle on discharge characteristics when a dual-frequency EAE waveform specified by equation (3) is employed. Throughout these studies the fundamental harmonic frequency is fixed at $f_1 = 13.56 \text{ MHz}$.

First we address the question of the proper choice of surface destruction probability (α) of oxygen singlet delta ($O_2(a^1\Delta_g)$) molecules. Due to the lack of data for different electrode materials and surface conditions, we varied this parameter to find the best overall agreement between the experimental and simulation data for ion fluxes at the electrodes. The best agreement was obtained using a value of $\alpha = 6 \times 10^{-3}$.

Before presenting our systematic study of the discharge characteristics using this fixed value of α , we illustrate the effect of varying α on several calculated characteristics of the discharge for a fixed set of operating conditions: $p = 100 \text{ mTorr}$, $\phi_{PP} = 150 \text{ V}$ and $N = 2$ (dual frequency excitation, ‘peaks’-type waveform). Figure 4(a) shows the influence of

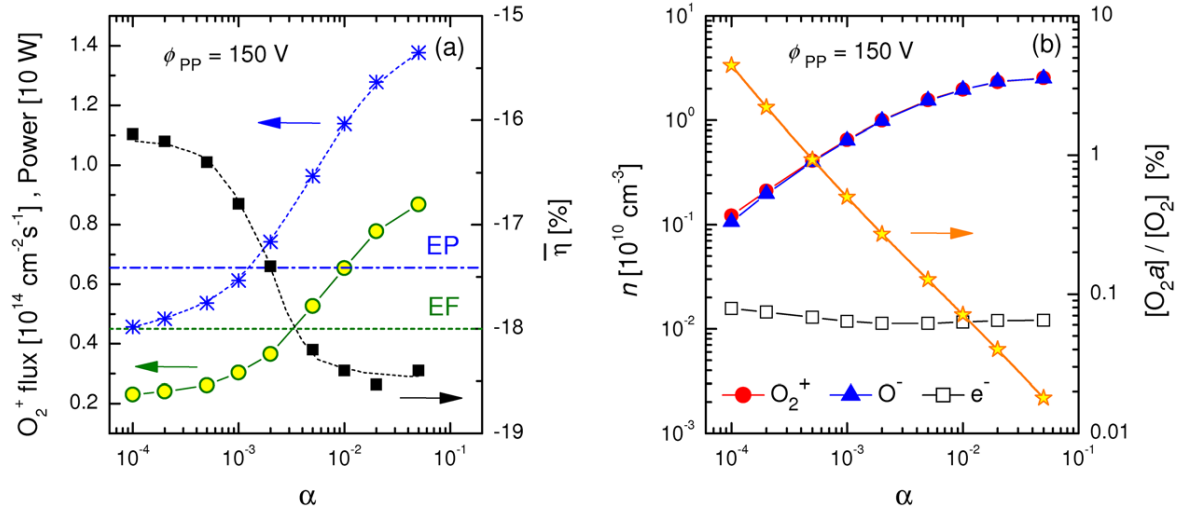


Figure 4. Dependence of the calculated (a) O_2^+ ion flux at the grounded electrode (line with circles; left scale), discharge power (dashed line with asterisks; left scale) and DC self-bias (line with squares; right scale), and (b) charged particle densities at the discharge centre and the $[O_2(a^1\Delta_g)]/[O_2]$ density ratio, on the surface destruction probability (α) of oxygen singlet delta ($O_2(a^1\Delta_g)$) molecules. The dashed horizontal lines in (a), marked ‘EF’ and ‘EP’, indicate the experimentally measured ion flux and discharge power, respectively. Conditions: $p = 100$ mTorr, $\phi_{PP} = 150$ V, $N = 2$.

the assumed value of α on the DC self-bias, calculated discharge power and O_2^+ ion flux (to the grounded electrode), while panel (b) presents the charged particle and $O_2(a^1\Delta_g)$ densities. The negative self-bias voltage increases from about 16–18.5% with rising α (see figure 4(a)). The surface destruction coefficient has a strong effect on the ion densities and, consequently, on the O_2^+ ion flux to the electrode. The O_2^+ ion density in the midplane of the discharge changes by a factor of >30 when the $O_2(a^1\Delta_g)$ surface destruction probability is scanned over the range $10^{-4} \leq \alpha \leq 5 \times 10^{-2}$. This implies a strong change of the electronegativity as well, since the electron density is nearly the same for all conditions. The $O_2(a^1\Delta_g)$ density decreases exponentially with increasing α . For the value of $\alpha \cong 6 \times 10^{-3}$, which was chosen in the rest of simulations, we find that for the conditions given here the $[O_2(a^1\Delta_g)]/[O_2]$ density ratio is in the order of $\sim 0.1\%$. This ratio, which changes by a factor of about three over the entire domain of the parameter space of our studies, is significantly lower than that assumed in [15], where a metastable to neutral density ratio of 1/6 was assumed. We note that a lower surface destruction coefficient $\alpha = 1 \times 10^{-5}$ and a correspondingly high $[O_2(a^1\Delta_g)]/[O_2] \approx 15\%$ density ratio was found in a study based on the experimental observation of spatiotemporal optical emission from the plasmas and a self-consistent 1D fluid model that included a semi-kinetic treatment of electrons [56], for similar discharge conditions as considered here. However, the surface properties of the stainless steel electrodes in [56], those in [15], and the (oxidized) aluminium used in our work are different. The exact nature of the electrode material and its surface conditions has been shown to have a significant effect on the surface destruction probability and, consequently, on the $O_2(a^1\Delta_g)$ density [56].

In figure 5, we illustrate the effect of discharge conditions and the number of driving RF harmonics on the self-bias of the

powered electrode. Here the bias is given as the normalized value, $\bar{\eta} = \eta/\phi_{PP}$. We find a very good agreement between the experimental data and the computed η values. The very low experimental values of η in the case of single-frequency operation ($N = 1$, which was only possible at the higher ϕ_{PP} values of 150V and 200V) confirm that the experimental system is highly symmetrical. For the ‘peaks’-type waveforms we find a negative bias, while ‘valleys’-type waveforms result in $\eta > 0$. The experimental data confirm that $\eta_{\text{peaks}} = -\eta_{\text{valleys}}$. We observe a monotonic increase of the magnitude of the self-bias with increasing number of harmonics, and the highest observed value of the normalized self-bias was $|\bar{\eta}| \approx 35\%$.

Figure 6 presents a comparison of the discharge power determined experimentally and in simulations. In both cases the power is determined from the period averaged product of the discharge voltage and discharge current. In the experiment the time dependent voltage $V(t)$ and current $I(t)$ signals, recorded on a digital oscilloscope, were multiplied and the power was derived from the time-averaged value of this product. The phase shift between voltage and current was taken into account. We note that a detailed phase and amplitude calibration of the current-voltage probe used in these measurements has been performed previously. More information on this calibration procedure can be found in [45]. In the simulations the discharge power was calculated from the time average of the $I(t) \cdot V(t)$ product, where $I(t)$ is the total current at a given (arbitrary) position within the gap (including the currents carried by electrons, positive and negative ions, as well as the displacement current) and $V(t)$ is the voltage applied to the powered electrode. The discharge power increases with the voltage amplitude as well as with increasing pressure and with increasing number of harmonics. In most cases the experiment and simulation agree to within a factor of two. For the case of molecular gases with complex plasma chemistry this agreement is acceptable considering the broad range of operation parameters.

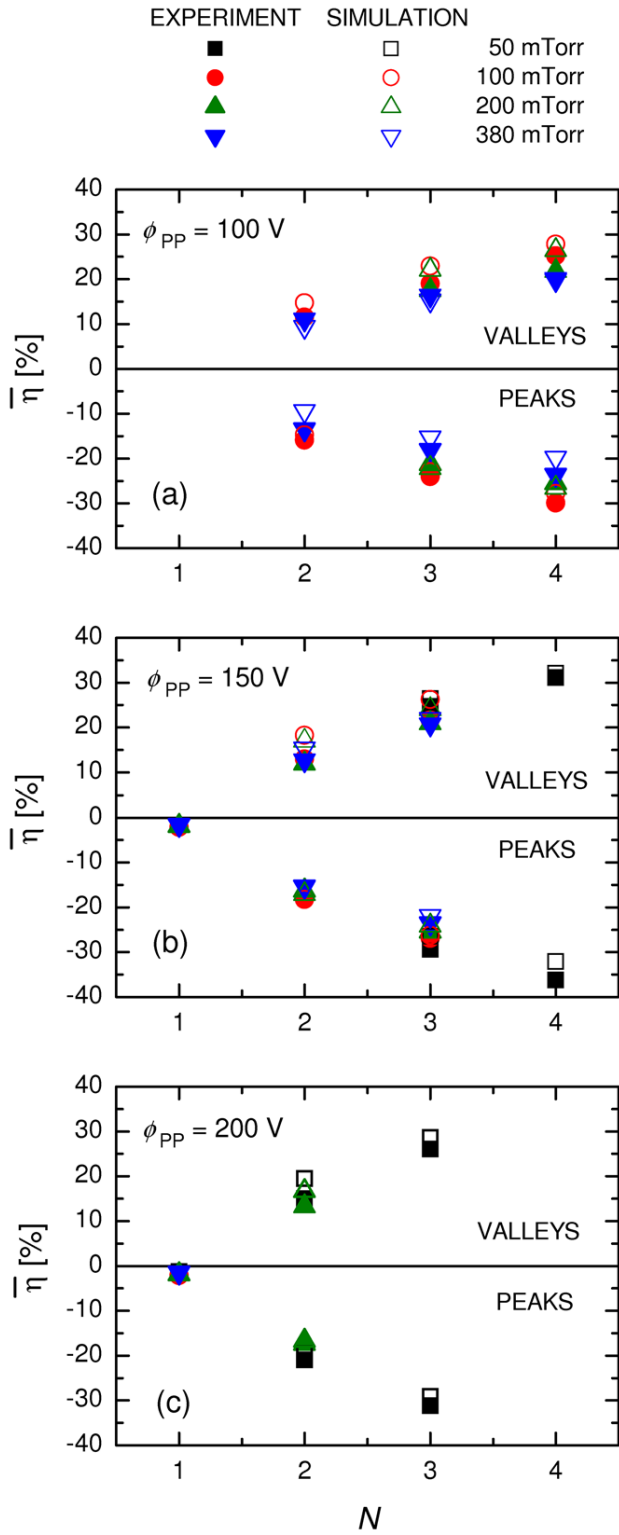


Figure 5. Normalized self-bias $\bar{\eta}$ as a function of the number of driving RF harmonics (N) for different voltage amplitudes (ϕ_{PP}), pressures and voltage waveform types.

The flux of O_2^+ ions to the grounded electrode is displayed in figure 7 for all operation conditions. The agreement between the experimental data points and the corresponding simulation results is fair in most cases, although for some conditions

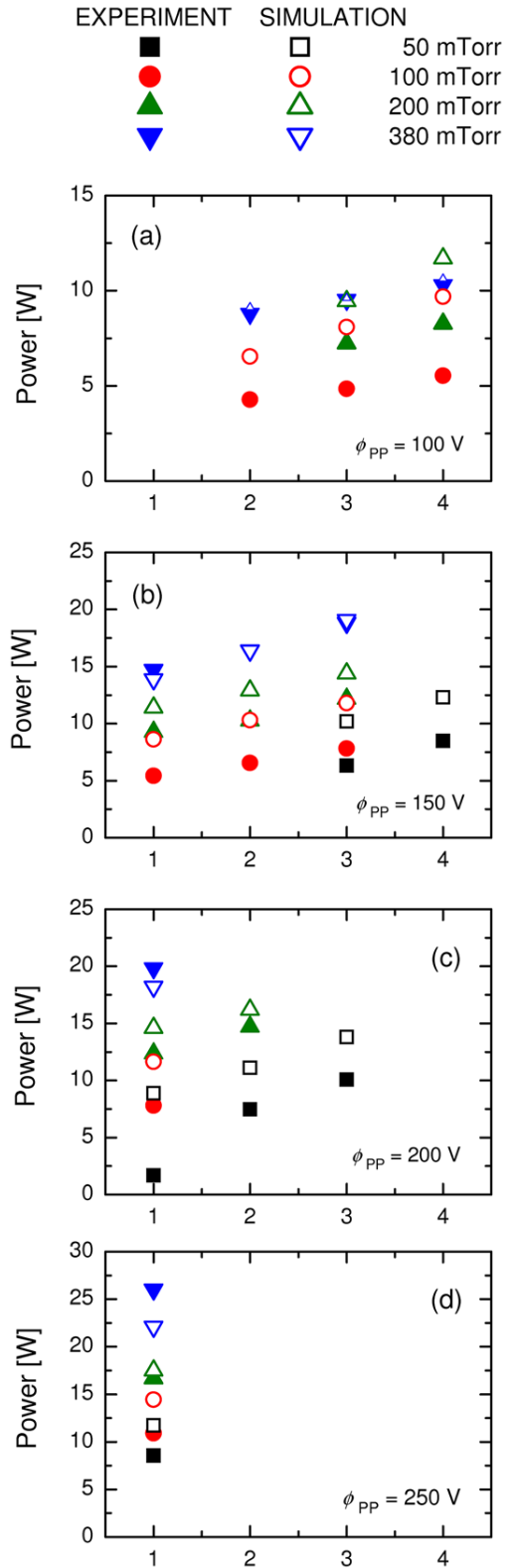


Figure 6. Discharge power as a function of the number of driving RF harmonics (N) for different voltage amplitudes (ϕ_{PP}) and pressures.

(e.g. in the low-voltage, high-pressure cases) a difference of up to a factor of three is seen. As figure 4 showed, the ion flux can be ‘tuned’ by a factor of up to four, by varying the surface

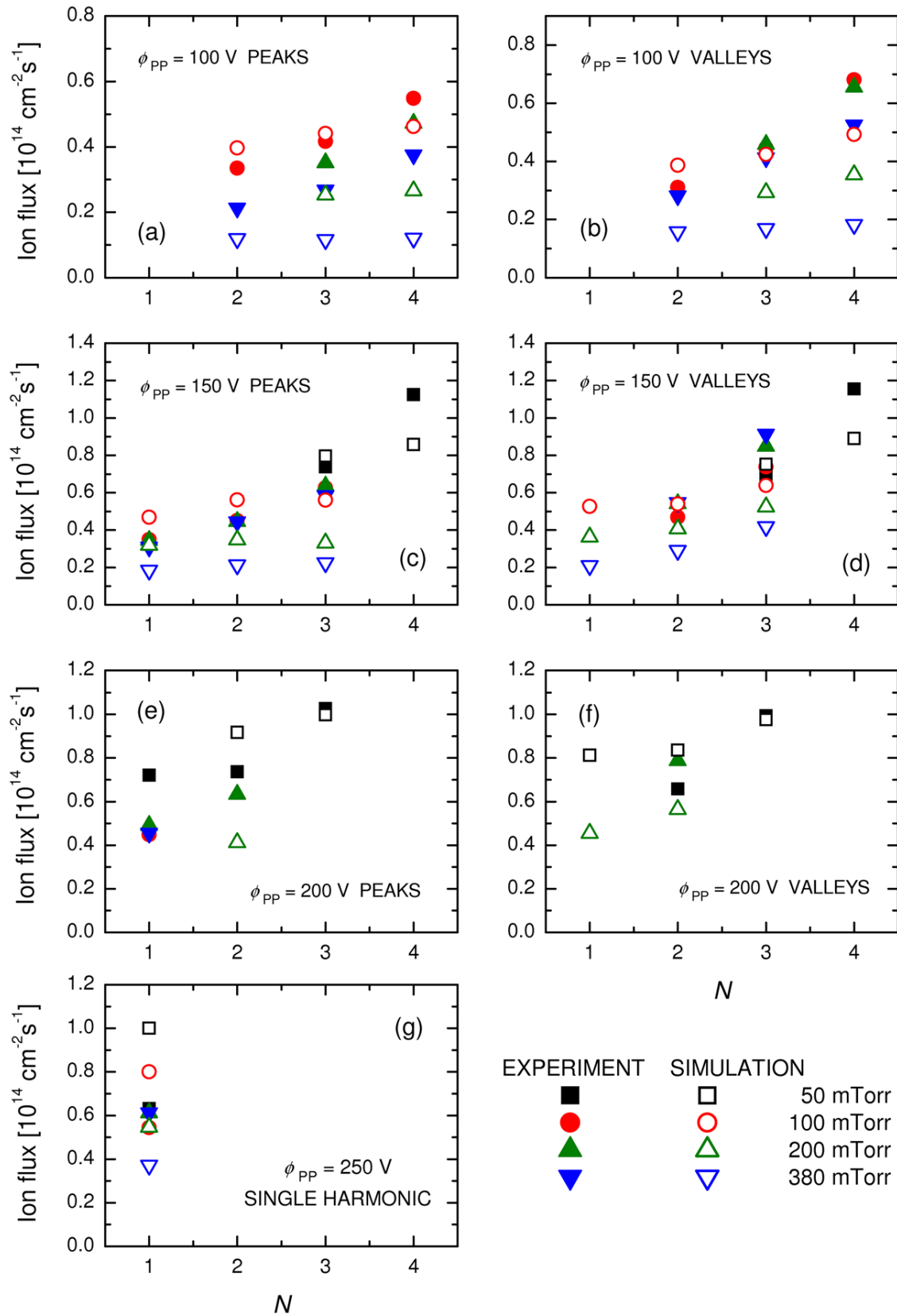


Figure 7. O_2^+ ion flux as a function of the number of driving RF harmonics (N) for different voltage amplitudes (ϕ_{pp}), pressures and voltage waveform types.

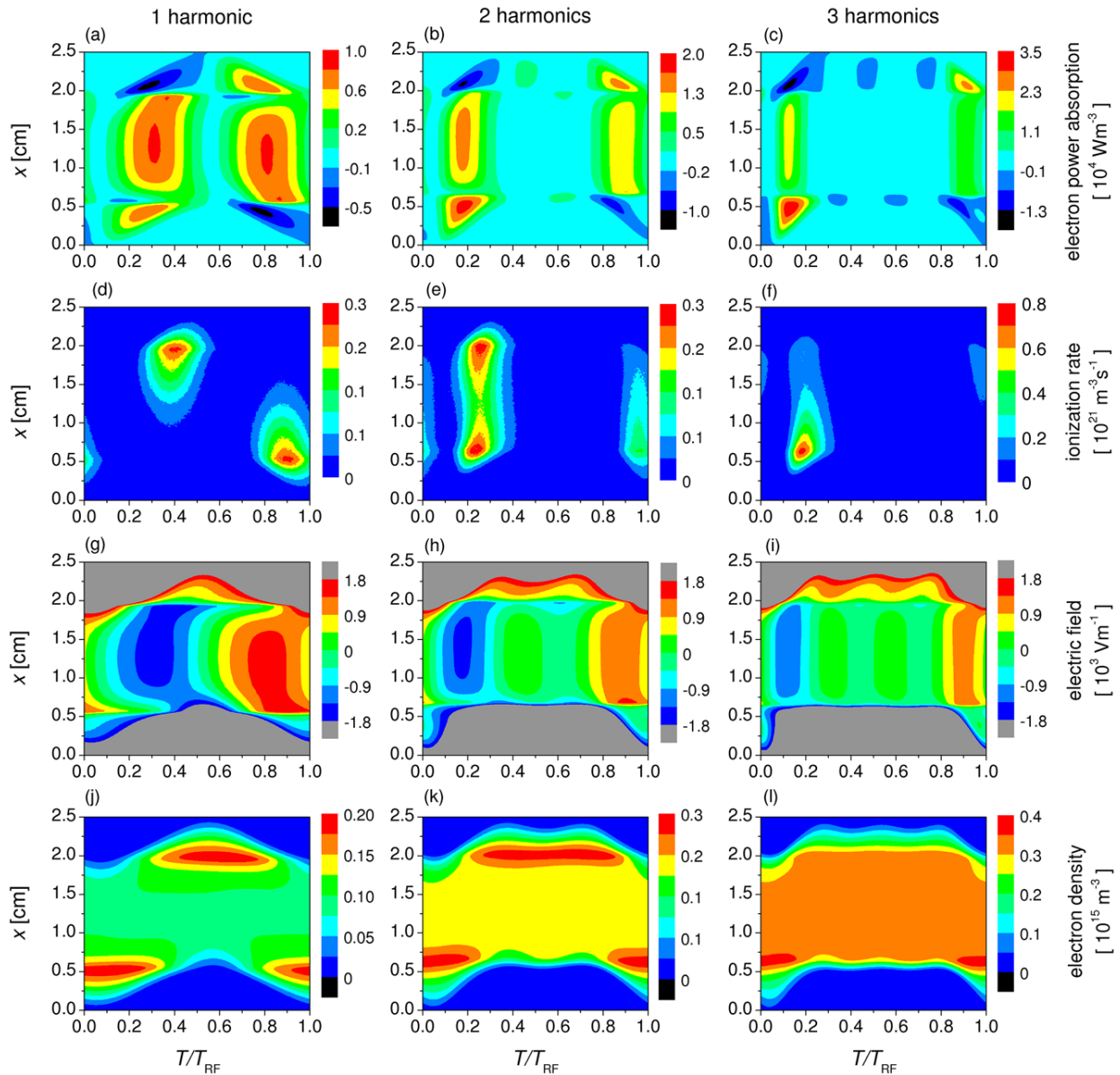


Figure 8. Spatiotemporal maps of the electron power absorption (row 1), rate of O_2^+ ion production (row 2), electric field (row 3) and electron density (row 4), for discharges operated with $N = 1, 2$ and 3 harmonics, ‘peaks’-type waveforms. $p = 200$ mTorr and $\phi_{\text{PP}} = 150$ V, $T_{\text{RF}} = 1/f_1$. The powered electrode is located at $x = 0$, while the grounded electrode is at $x = 2.5$ cm.

destruction rate (α) of $\text{O}_2(a^1\Delta_g)$. Therefore better agreement could have been achieved in these cases by choosing a different value of α in the simulations, but this would cause greater discrepancies under other conditions. It is clear that the $\text{O}^- + \text{O}_2(a^1\Delta_g) \rightarrow \text{O}_3 + \text{e}^-$ process plays a central role in the charged particle balance and a more refined model for the balance of the $\text{O}_2(a^1\Delta_g)$ molecules would probably give better agreement for the ion fluxes. This refinement is, however, left for future work, which would ideally be complemented by experimental measurements of the $\text{O}_2(a^1\Delta_g)$ density and kinetics.

The spatiotemporal behaviour of several discharge characteristics is shown in figure 8, for $p = 200$ mTorr and $\phi_{\text{PP}} = 150$ V. The maps show one period of the fundamental driving

frequency ($T_{\text{RF}} = 1/f_1$), with the position $x = 0$ corresponding to the powered electrode, while the grounded electrode is located at $x = 2.5$ cm. The figures show maps of the electron power absorption (row 1), rate of O_2^+ ion production (row 2), electric field (row 3) and electron density (row 4), for discharges operated with $N = 1, 2$ and 3 harmonics. For $N = 1$ we observe that the power absorption by the electrons is most significant in the bulk plasma (see figure 8(a)), where an electric field of ~ 15 Vcm^{-1} is generated (figure 8(g)) to drive the electron current at low electron density (i.e. to ensure current continuity [63]). In the presence of this field the electrons multiply significantly and the ionization rate is maximal near the edge of the collapsing sheath (figure 8(d)). At $N = 2$ the maximum of the electron power absorption moves nearer to

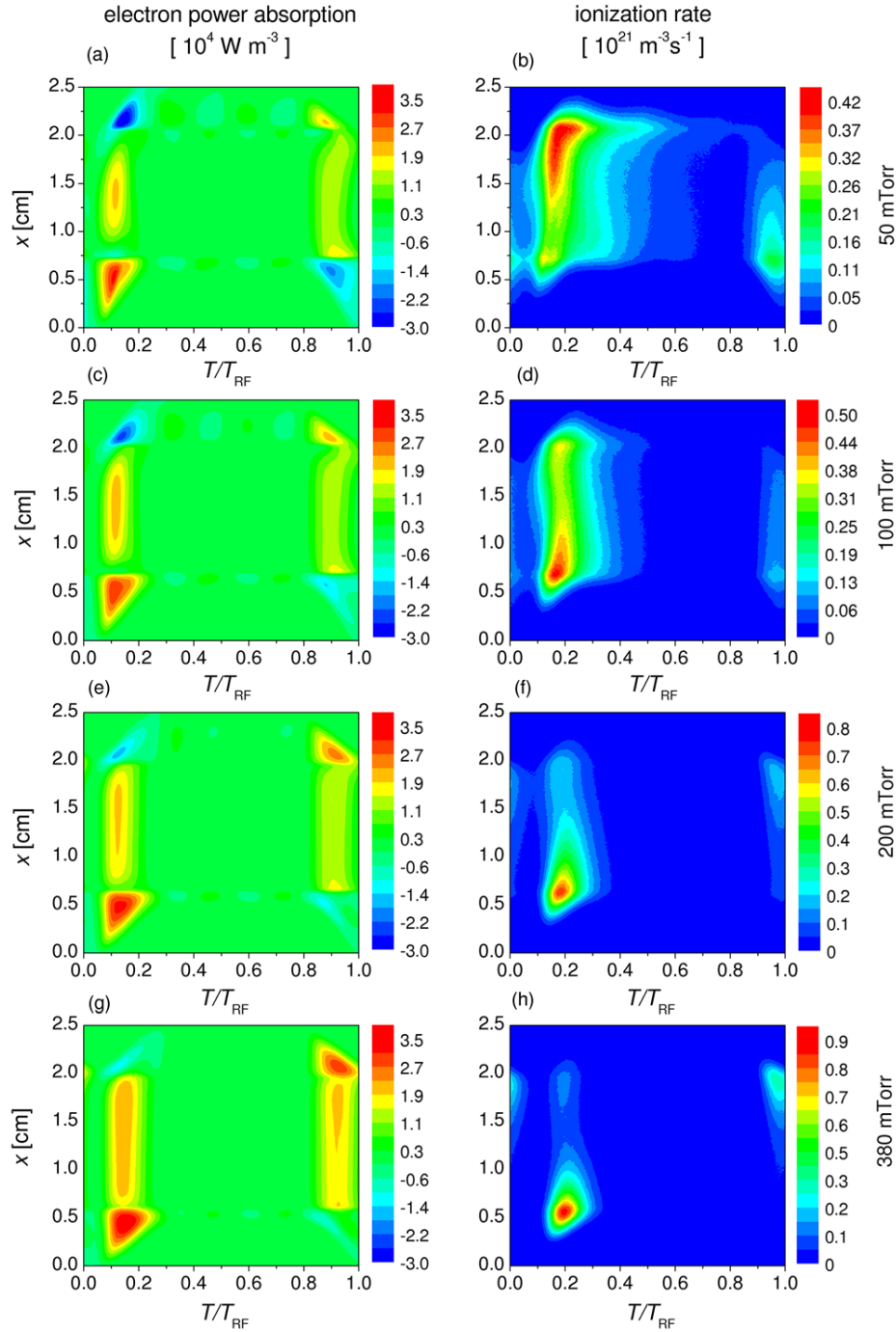


Figure 9. Spatiotemporal maps of the electron power absorption (row 1) and rate of O_2^+ ion production (row 2), for discharges operated at different pressures. $N = 3$ and $\phi_{pp} = 150$ V, ‘peaks’-type waveforms, $T_{RF} = 1/f_i$. The powered electrode is located at $x = 0$, while the grounded electrode is at $x = 2.5$ cm.

the edge of the expanding sheaths, especially at the powered side of the discharge, where the sheath expands much faster with dual-frequency driving voltage waveforms. As a consequence, at times of sheath expansion at the powered side, the ionization rate shows two maxima with nearly equal amplitudes, situated near the sheath edges at both sides (figure 8(e)), which originate from sheath expansion and sheath collapse, respectively. During sheath expansion at the grounded side

of the plasma, ionization is significantly weaker. This temporal asymmetry becomes even more significant for $N = 3$, where strong ionization is only present near the edge of the sheath at the powered electrode, and only during the expansion phase of the powered sheath (figure 8(f)). As the number of harmonics is increased, the heating mode changes from drift-ambipolar [63] at $N = 1$ to a classical alpha-heating mode at $N = 3$. During this heating mode transition the

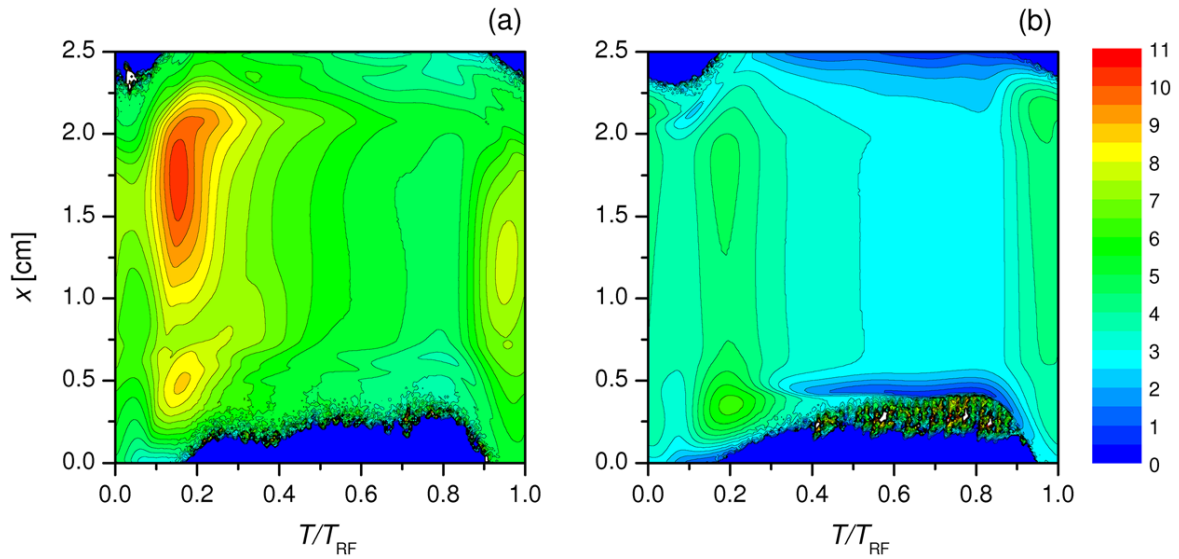


Figure 10. Spatiotemporal maps of the mean electron energy (given in eV) for $N = 3$ and $\phi_{PP} = 150$ V, for (a) $p = 50$ mTorr and (b) 380 mTorr. $T_{RF} = 1/f_1$. The powered electrode is located at $x = 0$, while the grounded electrode is at $x = 2.5$ cm.

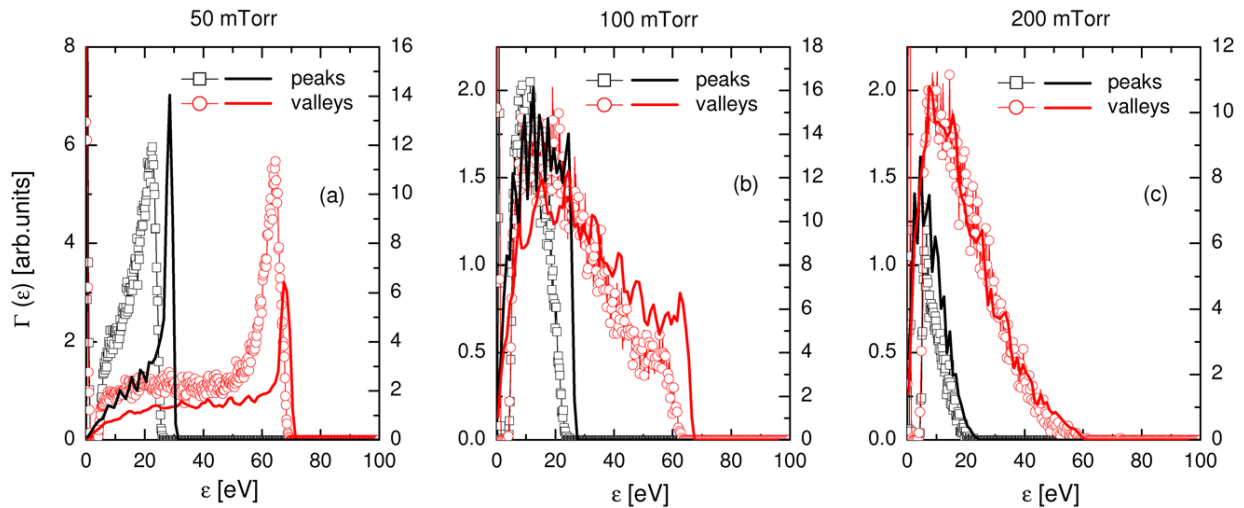


Figure 11. O_2^+ IFEDF at the grounded electrode of the discharge (given in arbitrary units), for ‘peaks’- and ‘valleys’-type waveforms, with $N = 3$ and $\phi_{PP} = 150$ V, for different pressures. Symbols represent the experimental data, while thick lines correspond to simulation results.

spatiotemporal profile of the electron density also changes, with electrons gradually filling the bulk region as the number of driving harmonics is increased (see figures 8(j)–(l)).

Besides the driving voltage waveform, gas pressure also considerably affects the electron dynamics and also induces a heating mode transition. Figure 9 shows spatiotemporal maps of electron power absorption and ionization rate for $N = 3$ and $\phi_{PP} = 150$ V, at different pressures. At the lowest pressure (50 mTorr) only weak ionization due to sheath expansion heating is found at the powered side, whereas electron acceleration and multiplication in the bulk plasma (DA-mode) gives rise to strong ionization in the bulk and in the vicinity of the collapsing sheath edge (figure 9(b)). As the pressure is increased (keeping the other conditions the same) the peak of the ionization rate shifts towards the powered sheath; at the highest pressure of 380 mTorr it

concentrates near the edge of the expanding powered sheath. The power absorption by electrons and ionization rate are much lower during sheath expansion phases at the grounded side of the discharge. Such transitions of the electron heating mode between α and drift-ambipolar modes have previously been observed in other electronegative gases, e.g. in CF_4 (see [64] and references therein).

The spatiotemporal distribution of the mean electron energy also changes significantly during the heating mode transition. The highest mean energy occurs at 50 mTorr, at $N = 3$ and $\phi_{PP} = 150$ V, conditions which favour the drift-ambipolar mode, see figure 10(a), (see figures 9(a) and (b)). Here, the highest mean energy (~ 11 eV) is reached in the bulk region. At a pressure of 380 mTorr this value decreases to ~ 5 eV, both in the bulk region and beyond the expanding sheath edge (figure 10(b)).

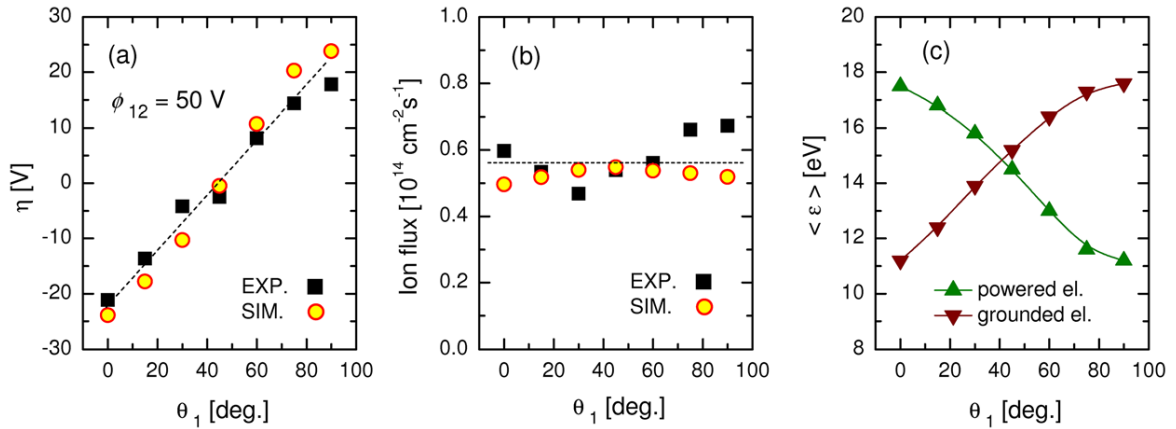


Figure 12. DC self-bias (a), ion flux at the grounded electrode (b), and mean ion energy at the powered and grounded electrodes (c) as a function of the phase angle Θ_1 between the two harmonics of the driving waveform (according to equation (3)), for $p = 100$ mTorr and $\phi_{12} = 50$ V.

The gas pressure also significantly influences ion dynamics. The shape of the IFEDF is determined to a large extent by the collisionality of the sheaths. Examples of the measured and calculated IFEDFs are displayed in figure 11, for $N = 3$ and $\phi_{pp} = 150$ V for different pressures. At the lowest pressure considered, the sheaths are only slightly collisional and the IFEDFs are characterized by a strong peak at the highest ion energy. At 100 mTorr, due to the higher number of collisions in the sheaths the IFEDFs peak at lower energies, while at an even higher pressure (200 mTorr) they show a faster decay at high energies. The measured and simulated distributions are in good general agreement, confirming that ion transport is handled reasonably correctly in the model. Note that, as mentioned in section 2, in the experiments the ion energy analyzer can be tuned nearly independently from the ion flux. For self-bias and ion flux, the computational results are compared with experimental data, and we find a very good agreement between the two sets of data.

Comparison of the present results in O_2 to those obtained for electropositive Ar discharges driven by tailored voltage waveforms reveals a number of similarities and differences. In both gases a DC self-bias is generated via the EAE for $N \geq 2$; this self-bias can be significantly increased by adding more consecutive harmonics to the driving voltage waveform with specific amplitudes. In contrast to Ar discharges, which often operate in the α -mode, where the sheath expansion heating dominates, O_2 discharges can operate in the drift-ambipolar mode, showing different spatiotemporal ionization dynamics. In this mode, electrons are heated in the plasma bulk by a high electric field, which is caused by the high electronegativity of the discharge, and these electrons induce strong ionization in the bulk. Further, at the collapsing sheath edge, ionization is generated by electrons accelerated by an ambipolar field due to the local maximum of the electron density in the electropositive edge region of the discharge. The drift-ambipolar operation mode, specific to electronegative discharges, affects the generation of the self-bias voltage and the control of process-relevant plasma parameters.

All the results presented so far were obtained with waveforms where all phase angles Θ_k were set either to 0 or π .

Varying these phase angles opens additional possibilities for controlling discharge properties. An important practical example is the case of dual-frequency excitation with a phase variation between the two harmonics, an excitation mode that has become known as the EAE [32, 62].

The panels of figure 12 show as a function of Θ_1 the DC self-bias voltage, ion flux at the grounded electrode, and mean ion energy at the powered and grounded electrodes, respectively, for $p = 100$ mTorr and $\phi_{12} = 50$ V. Changing Θ_1 from 0° to 90° results in a reversal of the self-bias, and thus influences the energy of the ions arriving at the electrodes, as shown in figure 12(c). Meanwhile the ion flux changes only slightly (see figure 12(b)), demonstrating that the ion energy can be tuned nearly independently from the ion flux. For self-bias and ion flux, the computational results are compared with experimental data, and we find a very good agreement between the two sets of data.

4. Summary

We have investigated capacitively coupled low pressure oxygen discharges driven by customized voltage waveforms. Several discharge characteristics, namely the self-bias voltage, power absorbed by the discharge, ion flux, and ion flux energy distribution have been determined both experimentally and via particle simulations. A comparison of these characteristics provided a thorough test of the collision-reaction model underlying the simulations. Very good agreement was found in terms of the DC self-bias values for all discharge conditions covered in the study. The discharge power and ion flux showed satisfactory agreement, considering the complex chemistry of the plasma and experimental errors. Good agreement was also found for the ion flux energy distributions at the electrodes.

The simulations give access to quantities that are not directly accessible experimentally. The spatiotemporal distributions of discharge characteristics (including the electric field, electron density, electron power absorption, ionization rate and mean electron energy) showed the transition between sheath expansion heating and drift-ambipolar modes. This

transition can be induced both by changing the number of harmonics comprising the excitation waveform or by the gas pressure.

An investigation of the dependence of the discharge characteristics on the surface destruction coefficient of the $O_2(a^1\Delta_g)$ singlet metastable molecules revealed the crucial role of these species via the $O^- + O_2(a^1\Delta_g) \rightarrow O_3 + e^-$ reaction, which strongly affects the negative ion balance of the plasma, and therefore the electron and ion densities and electronegativity. For all conditions studied the plasma was found to operate in the high-electronegativity mode, which is in accordance with the findings of [24] for low-voltage / low-power conditions.

A more detailed experimental characterization of the discharge plasma, involving measurement of the charged species densities in the bulk plasma and $O_2(a^1\Delta_g)$ density, as well as phase-resolved optical emission measurements, could aid in further refining the plasma chemistry model, leading to more reliable prediction of the different physical quantities characterizing oxygen discharges.

Acknowledgments

This work was supported by the Hungarian Fund for Scientific Research (OTKA) via grant K105476, and by financial support from the Agence Nationale de la Recherche project 'CleanGRAPH' (ANR-13-BS09-0019).

References

- Makabe T and Petrović Z Lj 2006 *Plasma Electronics: Applications in Microelectronic Device Fabrication* (London: Taylor & Francis)
- Chabert P and Braithwaite N 2011 *Physics of Radio-Frequency Plasmas* (Cambridge: Cambridge University Press)
- Jazbec K, Sala M, Mozetic M, Vesel A and Gorjanc M 2015 *J. Nanomater.* **2015** 346739
- Ko Y-M, Myung S-W and Kim B-H 2015 *J. Nanosci. Nanotechnol.* **15** 6048
- Chand U, Huang C Y, Jieng J H, Jang W Y, Lin C H and Tseng T Y 2015 *Appl. Phys. Lett.* **106** 153502
- Yin Z F, Sun L, Zou H L and Cheng E 2015 *Nanotechnology* **26** 215302
- Ham S W, Hong H P, Kim J W, Kim J H, Kim K B, Park C W and Min N K *J. Electron. Mater.* **44** 1344
- You Q H, Cai H, Gao K, Hu Z G, Guo S, Liang P P, Sun J, Xu N and Wu J 2015 *J. Alloys Compd.* **626** 415
- Birdsall C K 1991 *IEEE Trans. Plasma Sci.* **19** 65
- Verboncoeur J P 2005 *Plasma Phys. Control. Fusion* **47** A231
- Matyash K, Schneider R, Taccogna F, Hatayama A, Longo S, Capitelli M, Tskhakaya D and Bronold F X 2007 *Contrib. Plasma Phys.* **47** 595
- Vahedi V and Surendra M 1995 *Comput. Phys. Commun.* **87** 179
- Schuengel E, Zhang Q-Z, Iwashita S, Schulze J, Hou L-J, Wang Y-N and Czarnetzki U 2011 *J. Phys. D: Appl. Phys.* **44** 285205
- Gudmundsson J T, Kawamura E and Lieberman M A 2013 *Plasma Sources Sci. Technol.* **22** 035011
- Bera K, Rauf S and Collins K 2011 *IEEE Trans. Plasma Sci.* **39** 2576
- Lee M-H, Lee H-C and Chung C-W 2010 *Phys. Rev. E* **81** 046402
- Bronold F X, Matyash K, Tskhakaya D, Schneider R and Fehske H 2007 *J. Phys. D: Appl. Phys.* **40** 6583
- Dittmann K, Drozdov D, Krames B and Meichsner J 2007 *J. Phys. D: Appl. Phys.* **40** 6593
- Matyash K, Schneider R, Dittmann K, Meichsner J, Bronold F X and Tskhakaya D 2007 *J. Phys. D: Appl. Phys.* **40** 6601
- Benyoucef D and Yousfi M 2015 *Phys. Plasmas* **22** 013510
- Shibata M, Nakano N and Makabe T 1995 *J. Appl. Phys.* **77** 6181
- Liu J, Wen D-Q, Liu Y-X, Gao F, Lu W-Q and Wang Y-N 2013 *J. Vac. Sci. Technol. A* **31** 061308
- Liu J, Liu Y-X, Liu G-H, Gao F and Wang Y-N 2015 *J. Appl. Phys.* **117** 143301
- Descocudres A, Sansonnens L and Hollenstein Ch 2003 *Plasma Sources Sci. Technol.* **12** 152
- Küllig C, Wegner Th and Meichsner J 2015 *Phys. Plasmas* **22** 043515
- Küllig C, Dittmann K and Meichsner J 2010 *Plasma Sources Sci. Technol.* **19** 065011
- Teichmann T, Küllig C, Dittmann K, Matyash K, Schneider R and Meichsner J 2013 *Phys. Plasmas* **20** 113509
- Kitajima T, Takeo Y, Petrović Z Lj and Makabe T 2000 *Appl. Phys. Lett.* **77** 489
- Georgieva V, Bogaerts A and Gijbels R 2004 *Phys. Rev. E* **69** 026406
- Lee S H, Tiwari P K and Lee J K 2009 *Plasma Sources Sci. Technol.* **18** 025024
- Boyle P C, Ellingboe A R and Turner M M 2004 *Plasma Sources Sci. Technol.* **13** 493
- Rakhimova T V et al 2007 *IEEE Trans. Plasma Sci.* **35** 1229
- Waskoenig J and Gans T 2010 *Appl. Phys. Lett.* **96** 181501
- Turner M M and Chabert P 2006 *Phys. Rev. Lett.* **96** 205001
- Gans T, Schulze J, O'Connell D, Czarnetzki U, Faulkner R, Ellingboe A R and Turner M M 2006 *Appl. Phys. Lett.* **89** 261502
- Donkó Z, Schulze J, Hartmann P, Korolov I, Czarnetzki U and Schuengel E 2010 *Appl. Phys. Lett.* **97** 081501
- Heil B G, Czarnetzki U, Brinkmann R P and Mussenbrock T 2008 *J. Phys. D: Appl. Phys.* **41** 165202
- Donkó Z, Schulze J, Czarnetzki U, Derzsi A, Hartmann P, Korolov I and Schuengel E 2012 *Plasma Phys. Control. Fusion* **54** 124003
- Bienholz S, Styrnoll T and Awakowicz P 2014 *J. Phys. D: Appl. Phys.* **47** 065201
- Lafleur T, Delattre P A, Johnson E V and Booth J P 2012 *Appl. Phys. Lett.* **101** 124104
- Diomede P, Economou D J, Lafleur T, Booth J P and Longo S 2014 *Plasma Sources Sci. Technol.* **23** 065049
- Johnson E V, Delattre P A and Booth J P 2012 *Appl. Phys. Lett.* **100** 133504
- Franek J, Brandt S, Berger B, Liese M, Barthel M, Schuengel E and Schulze J 2015 *Rev. Sci. Instrum.* **86** 053504
- Schulze J, Schuengel E, Donkó Z and Czarnetzki U 2011 *Plasma Sources Sci. Technol.* **20** 015017
- Lafleur T, Boswell R W and Booth J P 2012 *Appl. Phys. Lett.* **100** 194101
- Bruneau B, Novikova T, Lafleur T, Booth J P and Johnson E V 2014 *Plasma Sources Sci. Technol.* **23** 065010
- Bruneau B, Gans T, O'Connell D, Greb A, Johnson E V and Booth J P 2015 *Phys. Rev. Lett.* **114** 125002
- Lafleur T 2015 Tailored-waveform excitation of capacitively coupled plasmas and the electrical asymmetry effect *Plasma Sources Sci. Technol.* at press
- Delattre P A, Lafleur T, Johnson E V and Booth J P 2013 *J. Phys. D: Appl. Phys.* **46** 235201

- [44] Patterson M M, Chu H Y and Wendt A E 2007 *Plasma Sources Sci. Technol.* **16** 257
- [45] Laffleur T, Delattre P A, Booth J P, Johnson E V and Dine S 2013 *Rev. Sci. Instrum.* **84** 015001
- [46] Hamers E A G, van Sark W G J H M, Bezemer J, Goedheer W J and van der Weg W F 1998 *Int. J. Mass Spectrom. Ion Process.* **173** 91
- [47] O'Connell D, Zorat R, Ellingboe A R and Turner M M 2007 *Phys. Plasmas* **14** 103510
- [48] Kutasi K, Guerra V and Sá P 2010 *J. Phys. D: Appl. Phys.* **43** 175201
- [49] Pinheiro M J, Gousset G, Granier A and Ferreira C M 1998 *Plasma Sources Sci. Technol.* **7** 524
- [50] Gudmundsson J T, Kouznetsov I G, Patel K K and Lieberman M A 2001 *J. Phys. D: Appl. Phys.* **34** 1100
- [51] Lazzaroni C, Chabert P, Lieberman M A, Lichtenberg A J and Leblanc A 2012 *Plasma Sources Sci. Technol.* **21** 035013
- [52] Turner M M 2015 *Plasma Sources Sci. Technol.* **24** 035027
- [53] Alves L L 2014 *J. Phys.: Conf. Series* **565** 012007
- [54] Midey A, Dotan I, Lee S, Rawlins W T, Johnson M A and Viggiano A A 2007 *J. Phys. Chem. A* **111** 5218
- [55] Midey A, Dotan I and Viggiano A A 2008 *J. Phys. Chem. A* **112** 3040
- [56] Greb A, Niemi K, O'Connell D and Gans T 2013 *Appl. Phys. Lett.* **103** 244101
- [57] Greb A, Gibson A R, Niemi K, O'Connell D and Gans T 2015 *Plasma Sources Sci. Technol.* **24** 044003
- [58] Biagi-v8.9 database 2014 (Cross sections extracted from PROGRAM MAGBOLTZ, VERSION 8.9 March 2010), www.lxcat.net, retrieved on November 25, 2014
- [59] Cunge G, Chabert P and Booth J P 1997 *Plasma Sources Sci. Technol.* **6** 349
- [60] Bzowski J, Kestin J, Mason E A and Uribe F J 1990 *J. Phys. Chem. Ref. Data* **19** 1179
- [61] Phelps A V 1994 *J. Appl. Phys.* **76** 747
- [62] Donkó Z, Schulze J, Heil B G and Czarnetzki U 2009 *J. Phys. D: Appl. Phys.* **42** 025205
- [63] Schulze J, Derzsi A, Dittmann K, Hemke T, Meichsner J and Donkó Z 2011 *Phys. Rev. Lett.* **107** 275001
- [64] Liu G-H, Liu Y-X, Wen D-Q and Wang Y-N 2015 *Plasma Sources Sci. Technol.* **24** 034006